Journal of Structural Biology 212 (2020) 107659

Contents lists available at ScienceDirect

Journal of Structural Biology

journal homepage: www.elsevier.com/locate/yjsbi

Investigation of the human pineal gland 3D organization by X-ray phase contrast tomography

Inna Bukreeva [a,b,*], Olga Junemann [c,*], Alessia Cedola [a,*], Francesca Palermo [a,d], Laura Maugeri [a,e], Ginevra Begani Provinciali [f,a], Nicola Pieroni [a,g], Alessia Sanna [a], Dmitry A. Otlyga [c], Alexey Buzmakov [h], Yuri Krivonosov [h], Denis Zolotov [h], Marina Chukalina [h,i], Anna Ivanova [h], Sergey Saveliev [c,1], Victor Asadchikov [h,1], Michela Fratini [a,e,1]

[a] Institute of Nanotechnology- CNR, Lecce Unit, Campus Ecotekne Via Monteroni, Lecce; Rome Unit, Piazzale Aldo Moro 5, Rome, Italy
[b] P.N. Lebedev Physical Institute, RAS, Leninskiy pr., 53 Moscow, Russian Federation
[c] FSSI Research Institute of Human Morphology, Tsyurupy Str 3, Moscow, Russian Federation
[d] Department of Physics, University of Calabria, I-87036 Arcavacata di Rende (CS), Italy
[e] IRCCS Fondazione Santa Lucia, Via Ardeatina 352, Rome, Italy
[f] Laboratoire d'Optique appliquée, ENSTA Paris, Institut Polytechnique de Paris, 828 boulevard des Maréchaux, Palaiseau, France
[g] SAIMLAL Department, Sapienza University, via A. Scarpa 14, Rome, Italy
[h] FSRC «Crystallography and Photonics» RAS, Leninskiy pr., 59, Moscow, Russian Federation
[i] Smart Engines Service LLC, 60-letiya Oktyabrya pr., 9, Moscow, Russian Federation

ARTICLE INFO

Keywords:
X-ray phase contrast imaging
X-ray micro-tomography
Human pineal gland
Pinealocytes
Pineal cysts
Pineal calcifications

ABSTRACT

Pineal gland (PG) is a part of the human brain epithalamus that plays an important role in sleep, circadian rhythm, immunity, and reproduction. The calcium deposits and lesions in PG interfere with normal function of the organ and can be associated with different health disorders including serious neurological diseases. At the moment, the detailed mechanisms of PG calcifications and PG lesions formation as well as their involvement in pathological processes are not fully understood. The deep and comprehensive study of the structure of the uncut human PG with histological details, poses a stiff challenge to most imaging techniques, due to low spatial resolution, low visibility or to exceedingly aggressive sample preparation. Here, we investigate the whole uncut and unstained human post-mortem PGs by X-ray phase contrast tomography (XPCT). XPCT is an advanced 3D imaging technique, that permits to study of both soft and calcified tissue of a sample at different scales: from the whole organ to cell structure. In our research we simultaneously resolved 3D structure of parenchyma, vascular network and calcifications. Moreover, we distinguished structural details of intact and degenerated PG tissue. We discriminated calcifications with different structure, pinealocytes nuclei and the glial cells processes. All results were validated by histology. Our research clear demonstrated that XPCT is a potential tool for the high resolution 3D imaging of PG morphological features. This technique opens a new perspective to investigate PG dysfunction and understand the mechanisms of onset and progression of diseases involving the pineal gland.

1. Introduction

The pineal gland (PG) is part of the human brain epithalamus located in the geometric center of the brain. This is a structurally complex asymmetric formation with average size of 1 cm^3 (Golan et al., 2002). The PG is a central structure in the circadian system, which produces melatonin under the control of the central clock and the suprachiasmatic nucleus (Erlich and Apuzzo, 1985). PG parenchyma is composed mainly of pinealocytes secreting melatonin, microglia and astrocytes. Calcium deposits are a common occurrence in human PG. They are progressively accumulated in PG tissue with age and are not usually considered as pathology (Koshy and Vettivel, 2001; Schmid, 1993). Recent studies on PG have shown that PG calcification can occur both outside and inside cells. Calcification was observed in PG matrix, and in the nucleus of

* Corresponding authors at: Institute of Nanotechnology – CNR, Rome Unit, Piazzale Aldo Moro 5, Rome, Italy (I. Bukreeva).
E-mail addresses: inna.bukreeva@cnr.it (I. Bukreeva), junemann@outlook.com (O. Junemann), alessia.cedola@cnr.it (A. Cedola).
[1] Equal contribution.

https://doi.org/10.1016/j.jsb.2020.107659
Received 26 June 2020; Received in revised form 19 October 2020; Accepted 20 October 2020
Available online 24 October 2020

pinealocytes (Kunz et al., 1999). Calcified tissue as well as cystic lesions and a variety of neoplastic, congenital masses and tumors in PG may interfere with normal PG function. Consecutively malfunctions of parenchyma cells secreting melatonin might be associated with sleep disorders, cancer, several psychiatric diseases, as well as neurodegenerative diseases, e.g. Parkinson's and Alzheimer's disease (Bruno et al., 2019; Kunz et al., 1999; Song, 2019; Tan et al., 2018). Up to the present time the detailed mechanisms of PG calcifications and PG lesions formation are not fully understood and many questions about the relationship between PG mass formation to neurosecretory cell pathologies and vascular network malfunctions remain unanswered.

Achieving a three-dimensional image of the whole human PG (characterized by a high degree of anatomical complexity) comparable in quality to histology poses a stiff challenge for most imaging techniques due to low spatial resolution, low visibility, or extremely aggressive sample preparation methods.

Thus, there is an increasing demand for a comprehensive study of the morphology of the whole PG at the level of cells and capillaries, using non-destructive, high-resolution 3D imaging techniques. In particular, the high-resolution visualization of degenerated tissues – inaccessible to standard 3D imaging techniques – would provide new opportunities for the understanding of the formation mechanisms of PG calcifications and lesions.

X-ray phase contrast tomography (XPCT) is based on both effects – the attenuation and the phase shift of the x-ray beam transmitted through a sample. It is capable to detect features in high and low absorbing biological tissue and analyze a sample at different scales: from whole-organ to cell structure. Recent publications (Bravin et al., 2013; Cedola et al., 2017; Fratini et al., 2015; Massimi et al., 2019) have demonstrated the ability of propagation-based imaging (PBI) to visualize the 3D architecture of the central nervous system – the neuronal and vascular networks, in particular – at micrometric and submicrometric scale. We applied PBI based XPCT as a relevant tool for 3D studies of uncut PG dissected from human post-mortem brain. PBI set-up exploits x-ray propagation in free space to visualize the internal structure of the sample and achieves high spatial resolution with a large field of view. Unlike standard imaging methods such as histology or CT, XPCT enables the high-resolution visualization of both x-ray transparent brain tissue and x-ray absorbing calcification (Fratini et al., 2015; Khimchenko et al., 2018; Massimi et al., 2019; Pacilè et al., 2019; Töpperwien et al., 2020) without destructive sectioning and without the need for exogenous contrast agents.

In this work, we studied the internal structure of four human PGs with different extent of intrapineal calcifications and PG cystic lesion using micro-CT, XPCT, and histology. Here we presented, to the best of our knowledge, the first nondestructive high-resolution 3D investigation of PG morphology at different scales: from the whole organ to cell. We identified macro- and microscopically different tissues such as parenchyma, vascular network, calcified tissue, and calcifications. XPCT findings have shown the presence of a cystic lesion in PGs invisible in micro-CT. Moreover, we observed the structural details of PG laminated calcifications and features characterizing the degradation of the pineal tissue in cystic PG. Specifically, we have distinguished the intact parenchyma including pinealocytes and tissue with a fibrous structure composed of glial cells processes replacing pinealocytes in cystic lesions. Based on our research, we believe that XPCT imaging would be an effective tool for a deep and comprehensive study of calcification and mass formation in PG and their relationship with pathologies and vascular network malfunctions.

2. Materials and methods

2.1. Samples

The post-mortem PG of four human subjects PG-I, PG-II, PG-III and PG-IV without neurodegenerative diseases have been collected and prepared to study the morphology and structure of the organ. In Table 1 we have reported the description of the samples including the name of the sample, gender and age.

The study was carried out on autopsy material obtained from the collection of Federal State Scientific Institution Research Institute of Human Morphology (Moscow, Russian Federation). All protocols were approved by the Ethical Committee of the Research Institute of Human Morphology of the Russian Academy of Medical Sciences (now FSSI Research Institute of Human Morphology) (No. 6A of October 19, 2009) and are in correspondence with instructions of the Declaration of Helsinki including points 7–10 for human material from 12.01.1996 with the last amendments from 19.12.2016.

2.2. Samples preparation for micro-CT and XPCT

Autopsy material (the whole pineal glands PG-I, PG-II, PG-III and PG-IV) was fixed in 10% formalin solution. Before performing the experiments, the samples were placed and maintained in 70% ethanol.

2.3. Micro-CT Set-up

Micro-CT measurements were performed at TOMAS microtomographic laboratory setup, developed and operating at the Federal Scientific Research Centre "Crystallography and Photonics" of Russian Academy of Sciences, described in detail in (Buzmakov et al., 2018). A standard x-ray tube with a molybdenum anode was used as a source. The values of the accelerating voltage and current were 40 kV and 20 mA, respectively. The energy of the probing radiation was 17.5 keV (pyrographite crystal was used as a monochromator). In each experiment, 400 radiography projections were measured in an angular range of 200 degrees with a step of 0.5 degrees. The measurements were carried out in parallel scanning scheme. Detector XIMEA xiRAY11 had a pixel size 9x9 micron, the total scan time was 120 min.

2.4. XPCT Set-up

XPCT measurements were performed using the Propagation Based Imaging (PBI) set up (Bravin et al., 2013). PBI exploits intensity variations via propagation of wave front between the object and the detector.

Samples PG-I and PG-II were measured at the ID17 beamline (ESRF) using a pink beam. The peak energy was 60 keV. The tomography was acquired in half-acquisition mode (Wang, 2002) with 3045 projections and an exposure time of 0.4 s, covering a total angle range of 360 degrees. Samples were placed at 1.2 m from the imaging system (Mittone et al., 2017) with pixel size of 3.5 μm.

PG-III and PG-IV were measured at the P05 beamline of the synchrotron facility PETRA III, DESY, operated by the Helmholtz-Zentrum Geesthacht (PETRA III, DESY) (Wilde et al., 2016) using a monochromatic beam energy 25 keV. The tomography was acquired in half-acquisition mode (Wang, 2002) with 4000 projections and an exposure time of 0.25 s, covering a total angle range of 360 degrees. Samples were placed at 0.5 m from the imaging system (Wilde et al., 2016) with pixel size of 1.28 μm and 0.64 μm.

2.5. Histology

The samples of human pineal glands PG-I, PG-II and PG-III were fixed

Table 1
Description of the samples.

Samples	Gender	Age, years
PG-I	F	79
PG-II	M	51
PG-III	F	70
PG-IV	F	69

in 10% buffered formalin. Fixed tissues were dehydrated in eight portions of absolute isopropyl alcohol IsoPrep (BioVitrum) and embedded in paraffin blocks. Ten-micron sections were cut and mounted on glass slices for Mallory's anillin blue connective tissue and Halocyanine staining.

2.6. Data processing and computational platform

We performed flat- /dark-fields correction on raw data and each tomographic projection was normalized with the average value of background outside the object. The phase contrast retrieval algorithm (Paganin et al., 2002) was applied to each XPCT projection. After the phase retrieval procedure, we used the resulting set of data for 3D reconstruction of the object. Tomographic reconstruction was done with Filtered Back Projection method (FBP). A post processing procedure has been applied to enhance visibility of calcifications and soft tissue of the PG. Standard tools and plugins of the open-source image program ImageJ/Fiji were used (Schindelin et al., 2012). In particular, average intensity and maximum intensity projection options of the standard tool "Z Project" of ImageJ/Fiji were used. Data pre-processing, artifact removal, phase retrieval and FBP reconstruction were done with the open-source software toolkit SYRMEP Tomo Project (STP) (Brun et al., 2017; van Aarle et al., 2015). Maximum projection through the XPCT volume with a thickness 10 μm has been used for the comparison with the histology, which is a 2D technique and the information in depth of histological section is averaged within 10 μm. Both maximum and average z-projections through XPCT volume with a different thickness has been applied to highlight specific 3D features in the samples.

3. Results

X-ray micro-CT, XPCT and histological technique were used to study the morphology of three post-mortem human PGs: PG-I, PG-II, PG-III. and PG-IV.

3.1. X-ray microtomography of PGs

Micro-CT technique was used to select the samples in terms of different extent and size of pineal calcifications. Fig. 1(a) shows an image of post-mortem human PG. Fig. 1(b) and 1(c) respectively display the 3D image of PG-I and PG-II, obtained in micro-CT experiments. Gray-scale reconstructed slices of PG-I and PG-II are shown in Fig. 1S(a-d) and 1S(e-h) of Supplementary Materials (SM), respectively. Segmentation of calcifications in PG-I and PG-II is shown in Fig. 1S(b,d) and 1S(f,h) of SM, respectively.

In Fig. 1(b,c) high absorbing calcifications are seen as white spots. Black spots, in Fig. 1(b,c), represent projections of the PG calcified area in three mutually orthogonal directions. In this regard, PG-I (Fig. 1(b)) has a minor degree of calcification and PG-II (Fig. 1(c)) shows a significant degree of calcification. In PG-III the intrapineal calcification was not detectable (the sample is not shown in the figure).

In Table 2 we have reported the PGs morphological characteristics obtained with micro-CT: pineal gland volume (PV), calcifications location (CaLoc), calcified volume (CaV), location of cysts (CyLoc), the total volume of cystic lesions (CyV), and active pineal volume (APV = (PV-(CaV + CyV))/PV).

We classified the calcified deposits based on their localization (pineal concrements localization CaLoc in Table 2). The main deposit of the concrements in PG-I was identified in the central part of the PG while the concrements of PG-II were concentrated in the central part as much as in the apical area of the epiphysis. Calcified deposits in PG-IV were identified mainly in the central part and the apex of the sample. We performed an evaluation of the PG volume (PV) and calcified volume (CaV) of the samples based on micro-CT. Volumes were segmented using global threshold binarization with a threshold of 0.4 mm^{-1} for calcifications and 0.078 mm^{-1} for PG soft tissue. The estimated PV of PG-I, PG-II, PG-III and PG-IV was about 246.7 mm^3, 104.2 mm^3, 98 mm^3, and 180 mm^3, respectively. The estimated CaV of PG-I, PG-II and PG-IV was about 5.2 mm^3, 13.2 mm^3, and 11.5 mm^3, respectively. The evaluation shows a significant extent of calcifications in PG-II reducing the Active pineal volume (APV) by 13%.

We noted that even if micro-CT imaging has provided high visibility of calcium deposits in the samples, however, detailed structure of the PGs soft tissue morphology including the cystic lesions could not be distinguished.

3.2. X-ray phase contrast tomography and histology in imaging of PGs

3.2.1. Pineal gland concrements

Fig. 2(a) and Fig. 2(c) show XPCT images of the whole PG-I (a) and PG-II (c), respectively. The images are the result of average intensity projection of 50 slices, corresponding to 150-μm thick sample (see Data processing and Computational platform in Materials and Methods). Gray-scale reconstructed slices of PG-I and PG-II are shown in Fig. 2S(a,

Table 2
Morphological characteristics of the samples: PV – pineal gland volume, Ca_Loc – calcifications location, Ca_V – calcified volume, CyLoc – location of cysts, CyV – total volume of cystic lesions, APV – active pineal volume.

Samples	PV, mm^3	CaLoc	CaV mm^3	CyLoc	CyV mm^3	APV
PG-I	246.7	Center	5.5	Center	0.3	0.98
PG-II	104.2	Center, apex	13.2	Non detected	Non detected	0.87
PG-III	98	Non detected	Non defined	Habenula region	7.5	0.92
PG-IV	180	Center apex	11.5	Non detected	Non defined	0.94

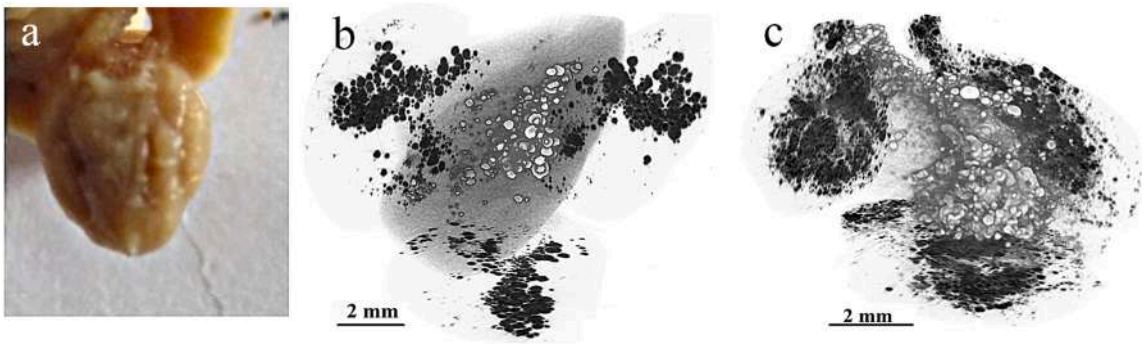

Fig. 1. (a) Photo of the human PG. (b) Micro-CT image of PG-I (c) Micro-CT image of PG-II Brain calcification is seeing as white spots. Projections of the PG calcified area in three mutually orthogonal directions are shown in figures (b) and (c) as black spots.

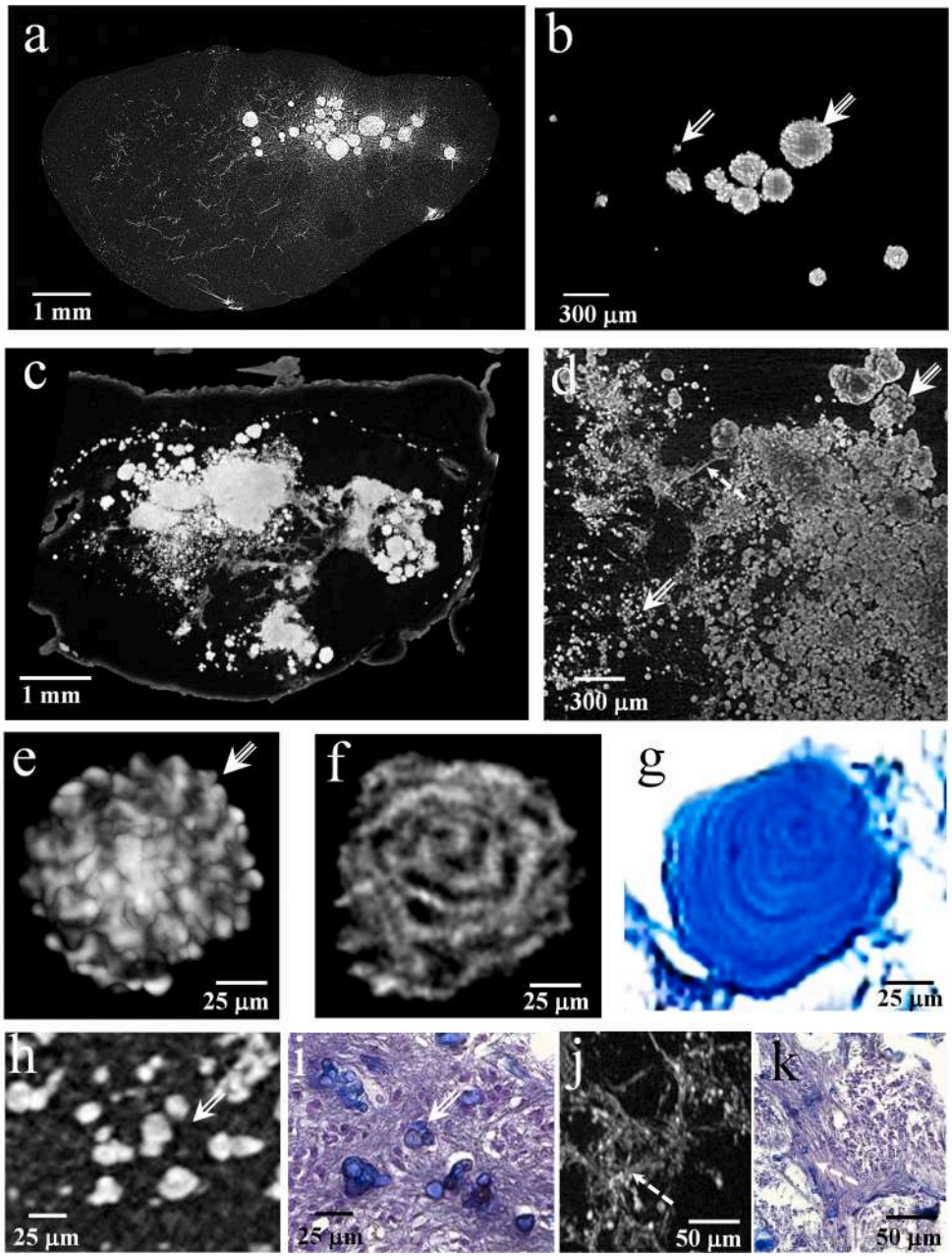

Fig. 2. (a) XPCT image of PG-I (b) Calcification in the internal part of PG-I. (c) XPCT image of PG-II. (d) Calcifications in the internal part of PG-II. (a-d) Images are obtained using the average intensity through a slab of 50 slices, corresponding to 150-μm-thick sample. (e) XPCT image of the mulberry shaped deposition in PG-II (white triple arrow). (f) Cross-section of the mulberry shaped deposition shown in (e). (g) Histological section of the concrement in PG-II, Mallory staining. (h) XPCT image of PG-II with non-aggregated and partially aggregated concrements (white double arrow). (i) Histological section of PG-II with calcifications, Mallory staining. (j) XPCT image of small-sized calcifications in the septa of PG-II (white dashed arrow). (k) Histology, small-size calcifications scattered over the septa of PG-II, Mallory staining. The thickness of the slabs in XPCT and histological images is about 10 μm.

b) and 2S(c,d) of SM, respectively. Major calcium deposits in both PG-I and PG-II are concentrated in the PG's matrix (intrapineal location) and some diffused calculi are scattered in the pineal capsule (extrapineal location). The zooms of PG-I and PG-II are shown in Fig. 2(b) and Fig. 2 (d), respectively. PG-I contains mainly non-aggregated concrements with mulberry shaped appearance (white triple arrow in Fig. 2(b)) concentrated in the central part of the PG and a few small-sized concrements (white double arrow in Fig. 2(b)) scattered in the PG matrix. PG-II contains a large amount of aggregated (white calcified conglomerates visible in Fig. 2(c,d)) and non-aggregated concrements (white triple arrow in Fig. 2(d)) of different sizes and shapes. Non-aggregated concrements were mainly detected in the periphery of PG-II.

A three-dimensional image of mulberry shaped concrement is shown in Fig. 2(e). The concrement has scallop-shaped concentric laminations in the internal structure, as shown in Fig. 2(f), which is in good agreement with histological section (Mallory staining; magnification of microscope ×200) given in Fig. 2(g). In both Fig. 2(f) and Fig. 2(g) the thickness of sections is about 10 μm. The mulberry-like concrements with laminar internal structure are typical for PG. Notably, the aggregation of multiple concrements can lead to large-scale lamination on the whole aggregate (Kim et al., 2012). An accumulation of spherical non-aggregated and partially aggregated concrements with a bumpy shape (white double arrow) formed in PGII are shown in the XPCT image (Fig. 2(h)) and in the corresponding histological section (Fig. 2(i)). Presumably, these friable concrements with their internal structure are provisional and can be destroyed during life.

The dense calcified conglomerates in PG-II, well seen in Fig. 2(c,d) as a massive white structure, and are the result of a multi-year's fusion of smaller aggregates. Apparently, concrements of this type are the most stable formations. The round shaped small-size mineral deposits scattered over the septa of PG-II are shown in Fig. 2(j) (XPCT image, white dashed arrow). The corresponding histological section is given in Fig. 2 (k).

3.2.2. *Pineal gland vascular network*

PG is a highly vascularized organ with a profusion of arteries, veins,

and capillaries (Goldman and Wurtman, 1964). The blood vessels enter the PG from the capsule via the connective tissue septa and form a dense network of interlobular capillaries, which drain into numeral pineal veins. Blood supply plays a fundamental role in PG melatonin secretion ability.

Rich vascularization has been detected in PG-I within the septa around the lobules and in the interlobular connective tissue, inside and outside the calcified area. The volume image of PG-I with a dense network of vessels segmented in red and calcifications segmented in white is shown in Fig. 3(a-c). Fig. 3 represents the axial (a) and longitudinal (b,c) view of PG-I obtained as a maximum projection through the volume with a thickness of about 0.5 mm. Fig. 3(d) comprises zooms of Fig. 3(a-c) showing the intrapineal vascular architecture with the profusion of PG blood vessels. Fig. 3(e-h) show XPCT (e,g) and histological (h) sections of a branching PG vessel with the well-seen lumen and the vessel wall. The diameter of the vessel is about 50 μm. The thickness of the wall is about 10 μm.

Fig. 4(a,b) illustrate the morphology of PG-II within the area of calcification. In these figures, calcifications (marked with white arrows) and fibrovascular stroma supporting the lobules (marked with yellow arrows) can be seen in white and are well distinguishable from the parenchyma, which is shown in dark. Yellow dashed arrows in Fig. 4(b) indicates the longitudinal section of PG trabeculae with well-seen lumen. Notably, the connective tissue image in Fig. 4(a,b) has a high contrast. This might indicate a high concentration of minerals in collagen that is consistent with the Ref. (Alcolado et al., 1986) where the authors found calcification of the choroid plexus stroma in the region of calcified depositions formation.

Morphological analysis, performed with XPCT and validated by histology, detected a few blood vessels in the calcification-free part of PG-II. In the highly calcified part of the sample we observed some vessels with calcium deposits along the walls. The three-dimensional XPCT images of a calcified vessel lumen is shown in Fig. 4(c). The longitudinal section of the vessel in Fig. 4(c) reveals the deposits attached to each other. The arrangement of the deposits is consistent with the shape of the vessel. The diameter of the vessel lumen is about 40 μm and the average size of the deposits is less than 10–20 μm. The histological image given in Fig. 4(d) shows a longitudinal section of blood vessels scattered with small concrements.

3.2.3. *Pineal gland soft tissue*

The PG has a complex morphology. The parenchyma of the pineal body composed of pinealocytes and neuroglial cells is surrounded by a connective tissue capsule composed of pia mater. From the capsule, the septa pass into the PG and divides the parenchyma into incomplete lobules.

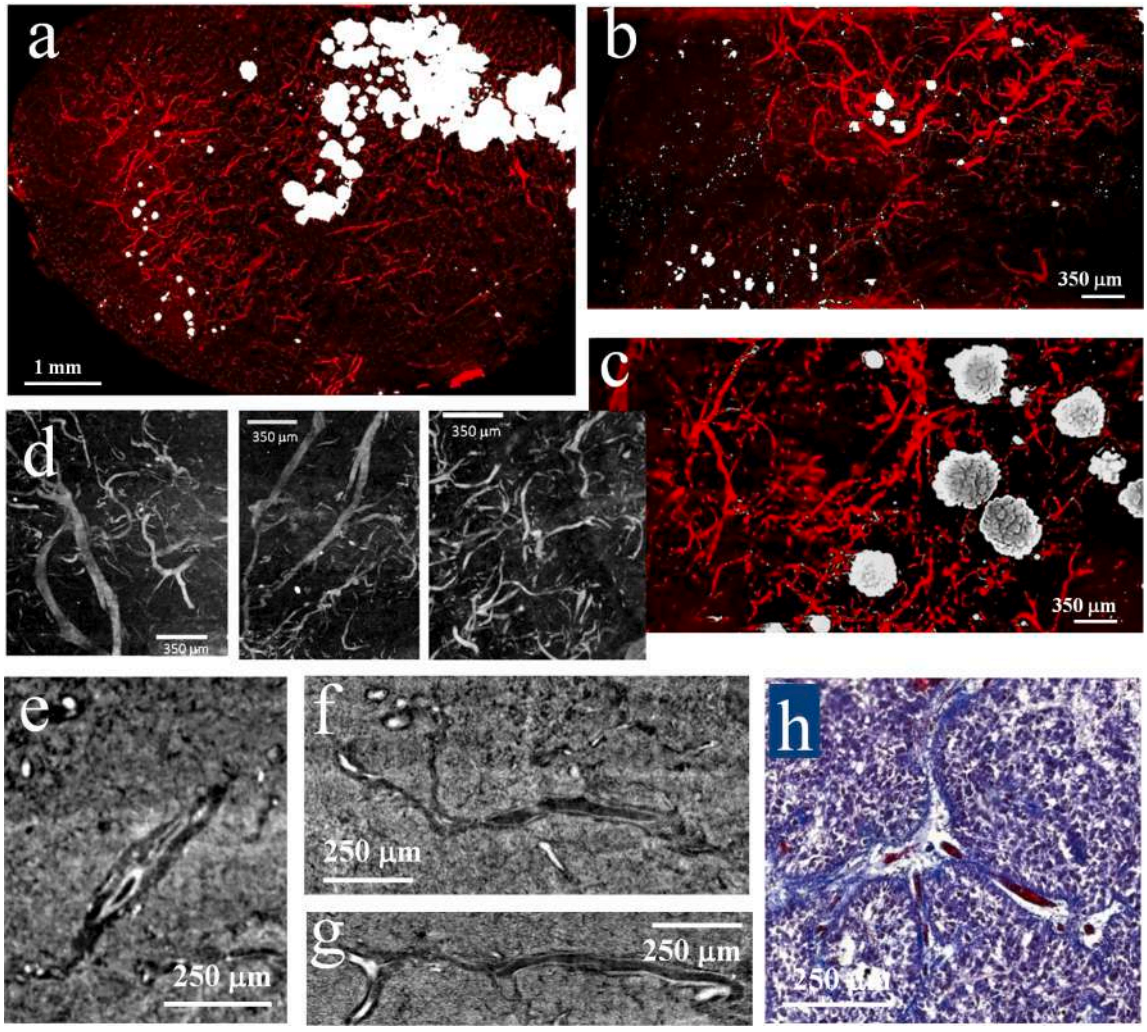

Fig. 3. A network of vessels revealed in PG-I. (a-g) XPCT image: (a) axial view and (b,c) longitudinal view of PG obtained as a maximum projection through the slab with the thickness of about 0.5 mm, calcifications segmented in white and blood vessels segmented in red; (d) zooms of the intrapineal blood vessels network shown in (a-c); (e-g) Images of the PG blood vessel with diameter of about 50 μm; (h) Histological section of the sample, Mallory staining. A branched vessel with uneven blood filling is visible. (For interpretation of the references to color in this figure legend, the reader is referred to the web version of this article.)

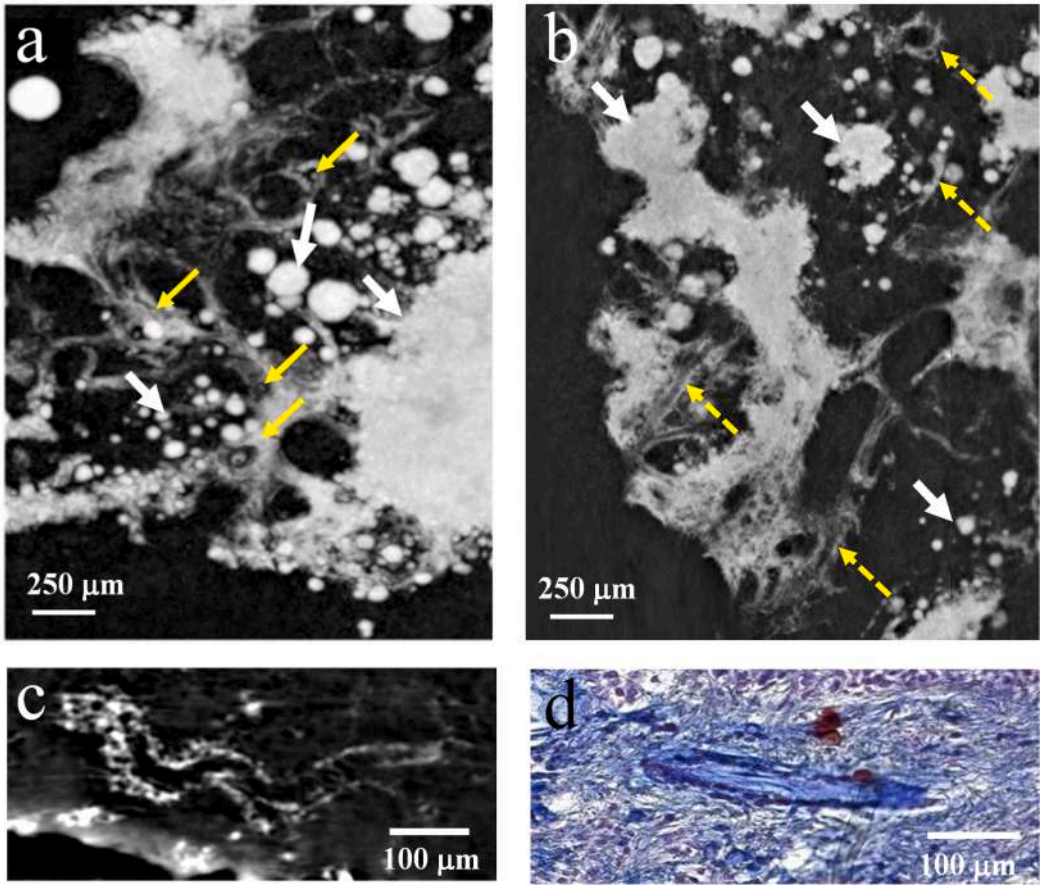

Fig. 4. XPCT image of PG-II. (a-b) Zoom of the central part: calcifications (marked with white arrows) and fibrovascular stroma supporting the lobules (marked with yellow arrows) are seen in white. The longitudinal section of PG trabeculae is marked with yellow dashed arrows. (c) The lLongitudinal virtual cut of the blood vessels scattered with calcium deposits. (d) Histological section of the blood vessel with lumen covered with calcium deposits, Mallory staining. (For interpretation of the references to color in this figure legend, the reader is referred to the web version of this article.)

Fig. 5(a,b) and Fig. 5(c,d) provide zooms of the central part of PG-I and PG-II, respectively, to better understand the organization of PG soft tissue within the area of concrements formation. Fig. 5(e,f) are the zoom of the peripherical part of PG-II. The left column in Fig. 5 represents the lobular architecture of samples (lobules are marked with blue arrows) obtained with XPCT imaging. The right column shows corresponding histological sections images. In Fig. 5(a) fibrovascular stroma supporting the lobules of PG-I are visible in dark gray , while blood vessels (marked with a red arrow) and small concrements are visible in white. In Fig. 5(c,e) calcifications and fibrovascular stroma of PG-II (the stroma is marked with yellow arrows) are visible in white and well distinct from the parenchyma visible in dark. The lobular structure in the peripheral part of PG-II (Fig. 5e, f) is damaged, the interlobular septa are strongly thickened.

Fig. 6(a) displays the histological image of the PG with multiple fluid-filled cysts diagnosed post-mortem in PG-I. The glial cyst (green arrow) with central coagulum and surrounding glial fibers (green double arrow) obtained with XPCT technique and histology are shown in Fig. 6 (b) and Fig. 6(c), respectively. The thickness of both the tomographic and the histological sections is about 10 μm (corresponding gray-scale reconstructed slice is shown in Fig. 2S(e) of SM). In Fig. 6(b), small blood vessels and intrapineal calcifications in area next to the cyst displayed as white spots cannot be distinguished from one another, while 3D image (thickness is about 200 μm) allows easy discrimination between blood vessels (red arrows in Fig. 6(b, d)) and calcifications (white spots in Fig. 6(d)). Three cysts observed in PG-I had a total volume of about 0.3 mm^3. Both, the cystic lesion and calcifications reduced active pineal volume (APV) of PG-I by 2% (see Table 2).

3.3. X-ray phase contrast tomography of PGs with high resolution

In sample PG-III both XPCT and histology identified glial cysts with the gliotic area that was invisible in the micro-CT image. The XPCT axial view of PG-III with the cystic lesion is shown in Fig. 7(a) (pixel size 1.28 μm). Gray-scale reconstructed slice of PG-III and zoom of the cyst are shown in Fig. 2S(f) of SM. The total volume of the cystic lesion is about 7.5 mm^3. Active pineal volume (APV) was reduced by 8%. (see Table 2).

To differentiate between the intact and degenerated PG tissue and increases the amount of information on the lesion morphology we used XPCT images with an enhanced spatial resolution (pixel size 0.64 μm) shown in Fig. 7(b,d) (a corresponding single slice of the sample is shown in Fig. 3S(a) of SM). One can clearly distinguish in Fig. 7(b) between intact PG parenchyma, where pinealocytes nuclei are visible as white dots, and the gliosis visible as a pinealocytes-less cyst wall composed of fibroblasts, glial cells and their processes. The histological section of the cyst (Mallory staining) is shown in Fig. 7(c). The structure of the gliotic area is represented in Fig. 7(d) (XPCT image, a corresponding single slice is shown in Fig. 3S(b) of SM) and Fig. 7(e) (histology, halocyanine staining). A good agreement between XPCT and histology results is evident. Images in Fig. 7(b,d) were retrieved as the maximum intensity projection of 15 slices, through the slab corresponding to the 10-μm-thick histological section.

The intrapineal vascular architecture of PG-III is shown in Fig. 8(a). Pineal gland vasculature is visible in the figure as a network of large, small and fine blood vessels (diameter of vessels varies from 1 to 100 μm). The image was retrieved as the maximum intensity projection through a 0.5 mm thick slab of the sample. Gray-scale reconstructed

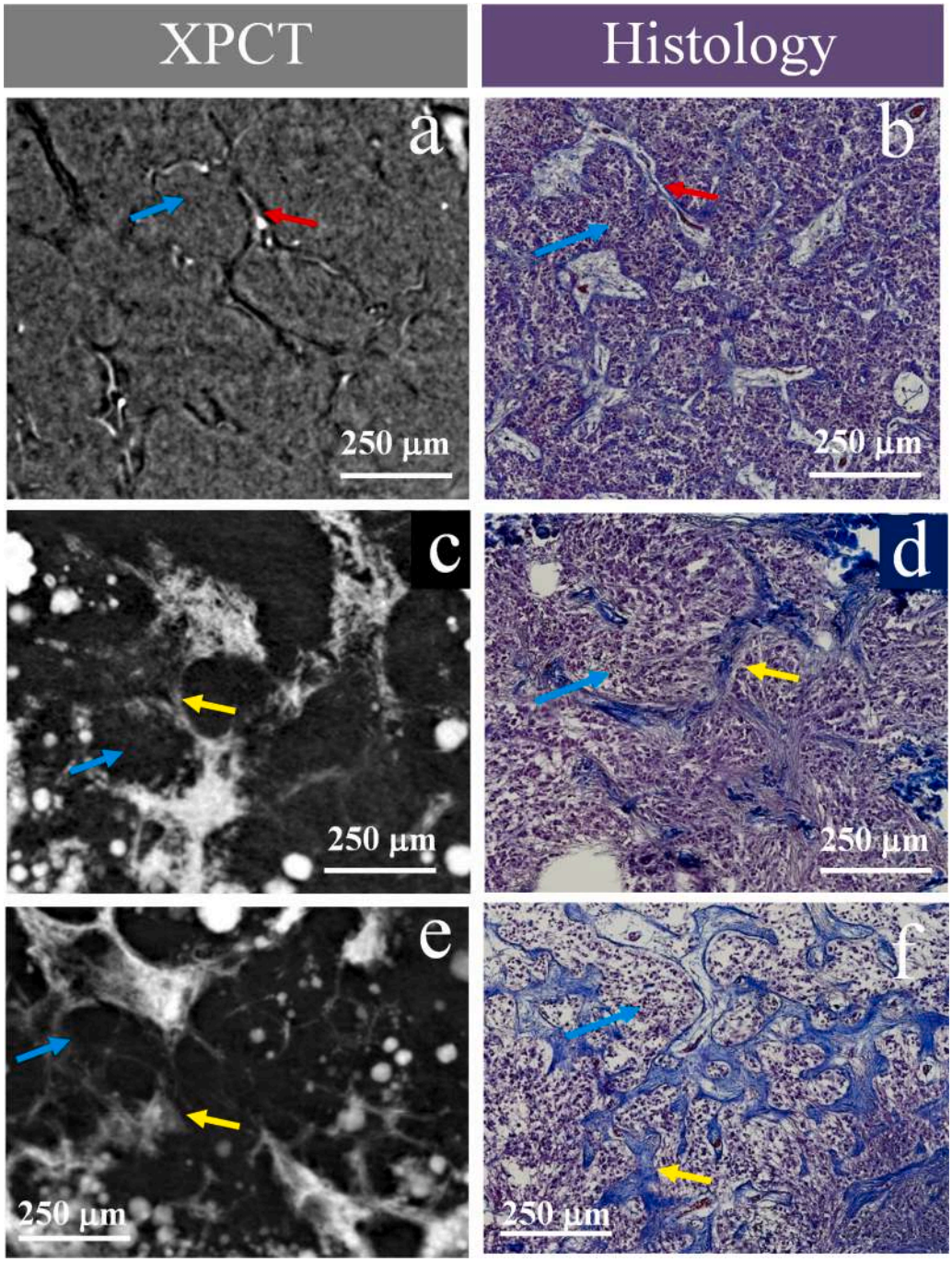

Fig. 5. PG parenchyma with the lobular architecture of samples. (a, b) The central part of PG-I: (a) XPCT images. (b) Histological section (Mallory staining) corresponding to (a). The lobular structure in (a, b) is partially damaged, the interlobular septa in some areas are strongly thickened. (c, d) The central part of PG-II. (c) XPCT images. (d) Histological section (Mallory staining) corresponding to (c). The lobular structure in (c, d) is damaged, calcified depositions are visible in the septa. (e, f) Peripheral part of PG-II. (e) XPCT images. (d) Histological section (Mallory staining) corresponding to (e). PG lobules, connective tissue septa and blood vessels are shown with blue, yellow and red arrows respectively. (For interpretation of the references to color in this figure legend, the reader is referred to the web version of this article.)

slices of PG parenchyma are shown in Fig. 3S(c,d) of SM. Fig. 8(b) represents XPCT image (10-micron-thick slab) illustarating PG parenchyma with fibrovascular stroma (yellow arrow), blood vessels (red arrow) and lobules with pinealocytes (blue arrow). Fig. 8(c) shows the corresponding histological section (Mallory staining) that has a good agreement with the tomography. Pineal gland cells are represented in Fig. 8(d). The pinealocytes in XPCT image are visible as a green cell's bodies with bright nuclei. The cells had an average diameter of about 9 μm. Their nuclei had an average diameter of about 6 μm. Histological image of cells obtained with halocyanine staining is shown in Fig. 8(e). The image of pinealocytes with processes surrounded by connective fibers is distinguishable in both Fig. 8(d) and Fig. 8(e).

XPCT image of the sample PG-IV is shown in Fig. 9(a) (pixel size 1.28 μm). Corresponding gray-scale reconstructed slice and segmentation of PG calcifications are shown in Fig. 2S(g) and 2S(h) of Supplementary Materials. In the sample both small separately lying concrements and calcifications combined into large conglomerates were detected. In Fig. 9a soft tissue and calcification are well distinguished. Fig. 9(b-g) illustrate the PG micro architecture with high resolution (pixel size 0.64 μm). Fig. 9(b) and 9(c) show 3D image and tomographic slice image of a separately lying concrement, respectively. The concentric laminations in the internal structure is well distinguished. A large conglomerate of calcifications is shown in Fig. 9(d). The cross-section shown in Fig. 9(e) reveals a noticeable large-scale lamination of the whole conglomerate.

Three-dimensional image and tomographic slice of a large conglomerate within the soft tissue are shown in Fig. 9(f) and 9(g), respectively (corresponding tomographic slice and segmentation of PG calcifications are shown in Fig. 3S(e) and 3S(f) of SM). The proliferation

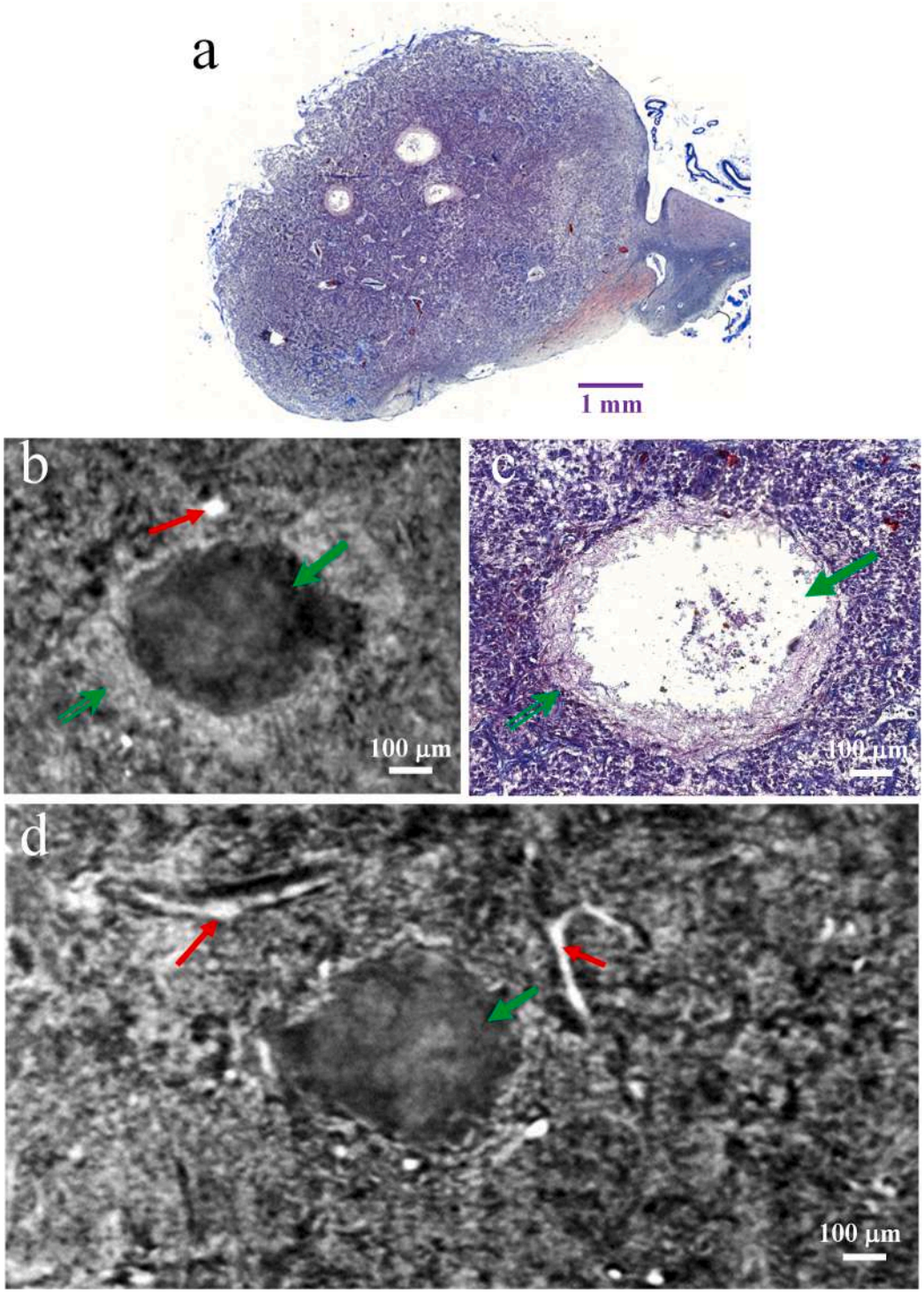

Fig. 6. Images of the cysts diagnosed post-mortem in PG-I. (a) Histological image (Mallory staining) of the PG with multiple fluid-filled cysts. (b) XPCT image of the cyst surrounded by glial fibers, thickness of the slice is about 10 μm. (c) Histological section (Mallory staining) of the cyst, surrounded by glial fibers. (d) XPCT image of the PG with the cyst (thickness of the slice is about 100 μm). The glial cyst is marked with green arrows while the glial fibers surrounding the cyst are marked with green double arrows, and small blood vessels are marked with red arrows. (For interpretation of the references to color in this figure legend, the reader is referred to the web version of this article.)

of connective tissue in the parenchyma is noticeable. Pinealocytes nuclei and blood vessel network are well seen. A network of capillaries with uneven blood filling is detected.

4. Discussion

We used synchrotron-based free space propagation XPCT imaging to perform 3D virtual histology on human PG. Unlike the standard histological method, XPCT allowed us to visualize the principal morphological features of the whole PG without destructive sectioning of samples and exogenous contrast agents. We displayed in 3D with near-histological quality the PG lobular structure and pinealocytes surrounded by connective tissue spaces, PG vascular network and calcifications of varying size embedded in a PG soft tissue. In addition, we detected PG lesions and visualized the degenerated tissue fine structure invisible in micro-CT. These results were confirmed by histological examinations.

In PG-I we observed rich vascularization and a relatively small quantity of PG concrements, which were mainly concentrated in the central part of the PG. On the one hand, both micro-CT and XPCT images of PG-I have shown relatively small APV reduction in the sample due to calcification. On the other hand, XPCT images revealed additional APV

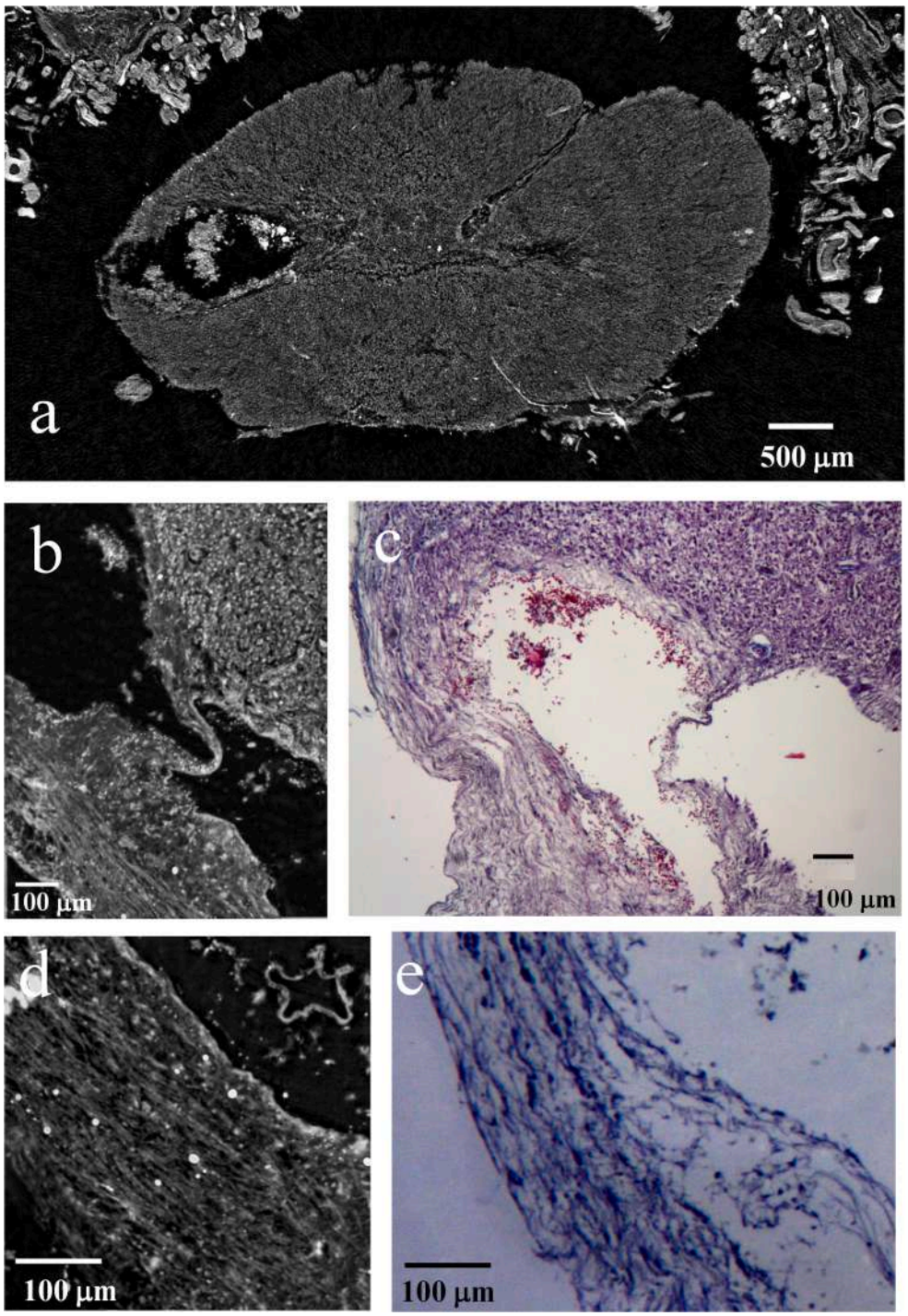

Fig. 7. Images of the cyst diagnosed post-mortem in PG-III. (a) XPCT image of the whole sample with a large cystic lesion. (b) XPCT image of the cyst surrounded by glial tissue. (c) Histological section of the sample with the cyst, Mallory staining. (d) The structure of the glial tissue, XPCT image. (e) Glial tissue, histological section, halocyanine staining. Thickness of both XPCT and histological sections is about 10 μm.

reduction due to multiple benign PG glial cysts in PG-I invisible in micro-CT.

In PG-II we observed extended intrapineal calcified depositions of various sizes, scattered overall the organ. In particular, massive calcifications were observed in the center and in the apex of the PG, in correspondence with histology. XPCT image analysis of PG-II within and outside the area of calcifications formation showed multiple calcified vessel lumens, both smooth walls and walls completely covered with calcified depositions were observed. The pathological appearance of the vessels suggests poor blood supply of the organ. Moreover, XPCT analysis revealed a potentially high calcium concentration in the collagen of the fibrovascular stroma. We hypothesized that the vessels and stroma pathology may be correlated with the formation of the extended intrapineal calcifications in PG-II.

In PG-III we observed two large glial cysts surrounded by a rim of a glial tissue that reduced APV. Three-dimensional image, with a resolution near to 1 μm, allowed clearly distinguishing between the intact PG parenchyma composed by pinealocytes and the pinealocytes-less area composed by fibroblasts, glial cells and their processes. By means of the 3D image we also distinguished the pinealocytes structure including cell

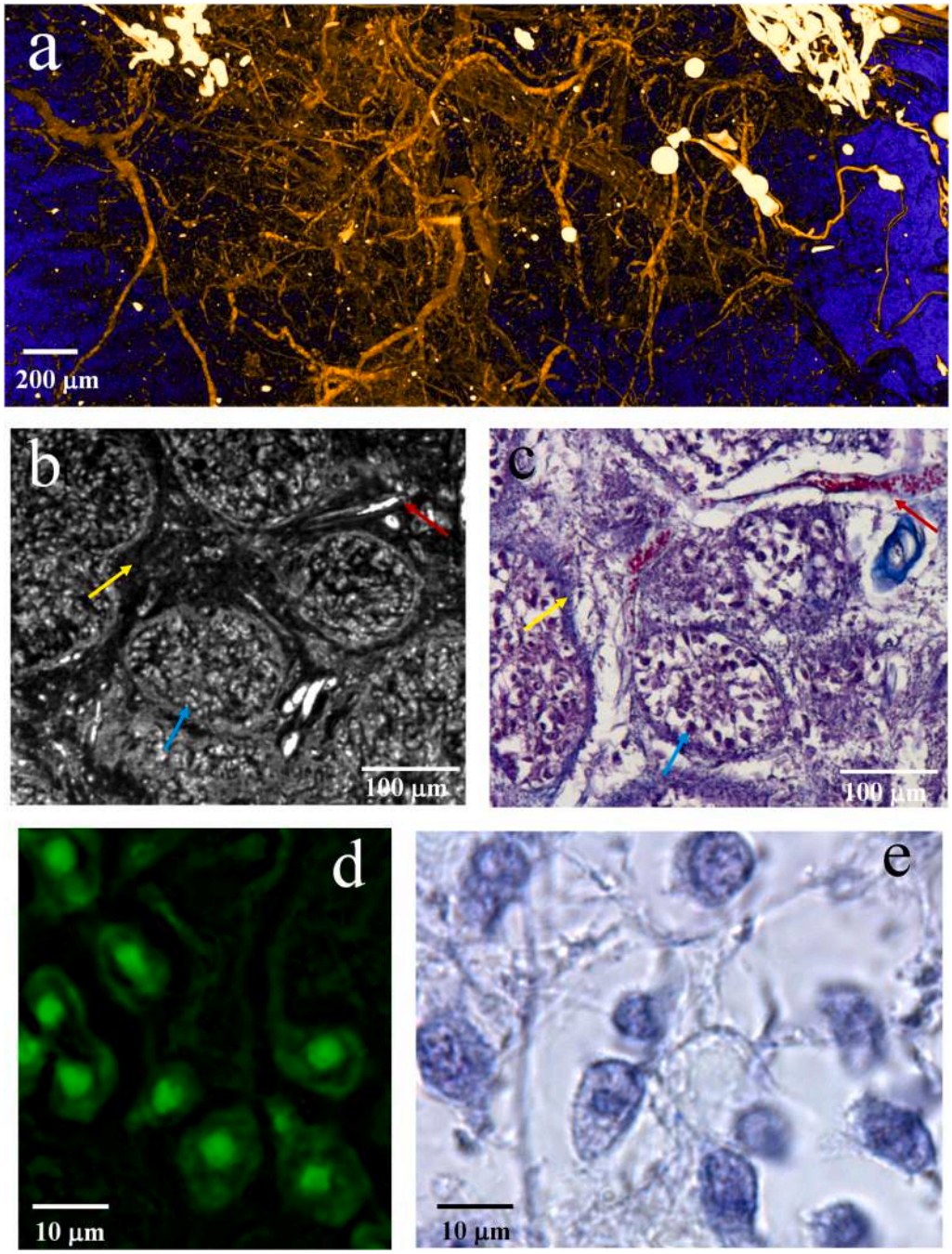

Fig. 8. Morphology of PG-III: (a) The intrapineal vascular architecture of the sample, XPCT image of 0.5 mm thick slab. (b) PG lobular structure, the area of parenchyma with fibrovascular stroma (yellow arrow) blood vessels (red arrow) and lobules with pinealocytes (blue arrow), XPCT image of the 10-μm-thick slab. (c) Histological section with PG lobular structure, Mallory staining, objects and color of arrows corresponds to (b). (d) XPCT image of pinealocytes visible as a green cell's bodies with bright nuclei. (e) Histological image of the pinealocytes with processes surrounded by connective fibers, halocyanine staining. (For interpretation of the references to color in this figure legend, the reader is referred to the web version of this article.)

bodies and nuclei. Besides, we segmented a network of PG microvessels.

In PG-IV both, small separately lying concrements and calcifications combined into large conglomerates were detected. Improved image resolution (pixel size 0.64 μm) allowed to distinguish the microarchitecture of the concrements with concentric lamination in the internal structure. In large conglomerates of calcifications a noticeable large-scale lamination of the whole conglomerate was revealed.

However, we noted that the micron resolution was insufficient to resolve the features of neural and capillary networks that are important in the understanding of PG dysfunctions. Recent studies on PG have shown that PG calcification can occur both outside and inside cells (Kunz et al., 1999). The problem of PG ultra-structure visualization can be solved with a sub-micron spatial resolution experiment that is the next challenge to be dealt.

The samples were examined under different experimental conditions i.e. different incident energies (monochromatic and pink beam energy), different embedding material (air, agarose gel and paraffin) and different spatial resolutions (pixel from 3.5 μm to 0.64 μm), to attain an acceptable quality of high-resolution 3D imaging of both PG soft tissue and calcifications and their microstructure. We summarized the results as follows: incident monochromatic energy of about 25 provides good quality visualization of both soft tissue and concrements; the best results were obtained in paraffin embedding material; one of the main challenges in the 3D visualization of PG was image artifacts.

The critical issue to consider in the 3D imaging of PG is the artifacts generated by the strong-absorbing calcified concrements in the sample. In some areas of the samples with extensive multiple calcifications, the artifacts significantly degrade the quality of images. The problem may be eventually overcome by the future improvement of computational algorithms and the optimization of experimental methods and

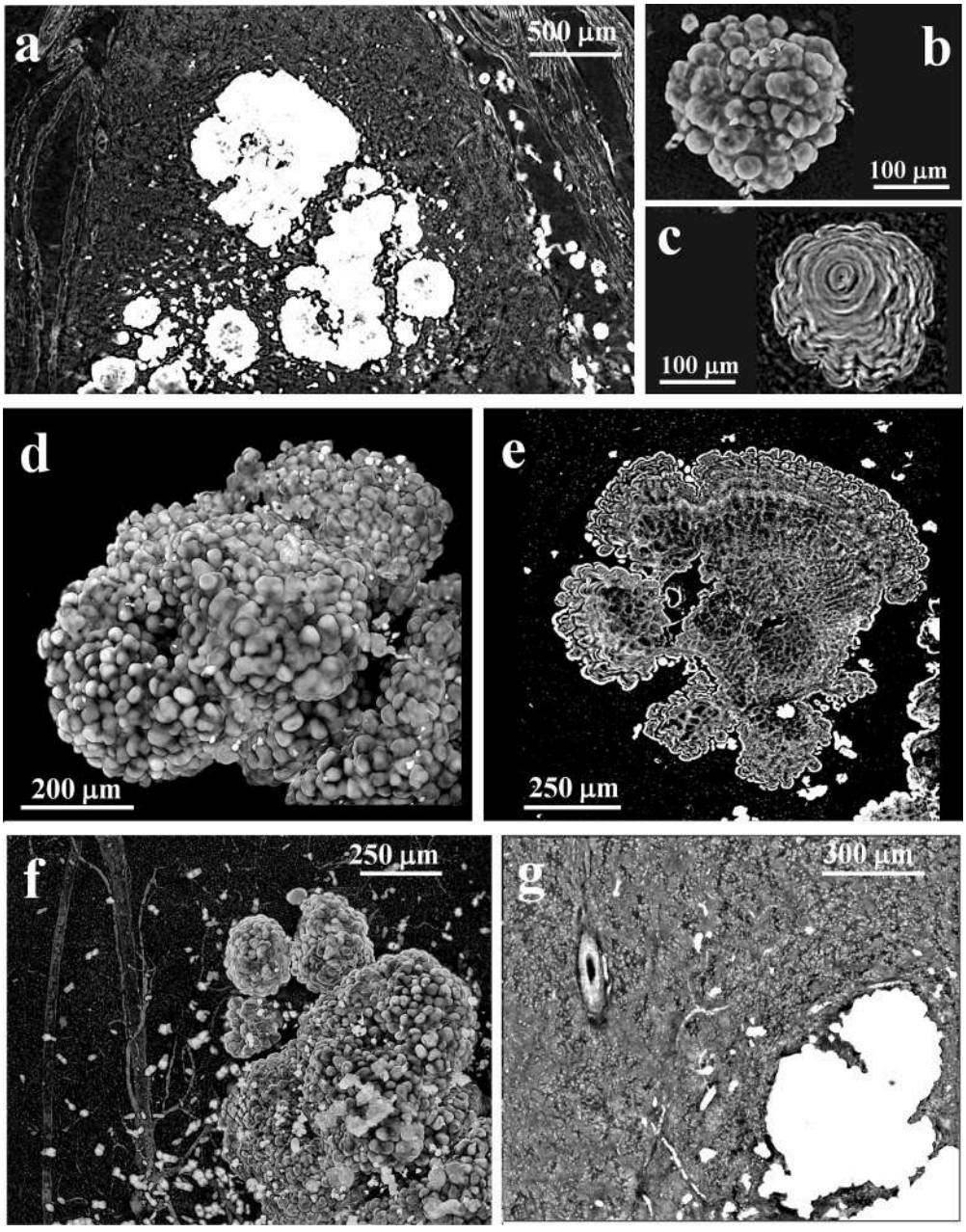

Fig. 9. XPCT image of the sample PG-IV. (a) PG-IV tomographic slice (pixel size 1.28 μm). (b) 3D image of a calcification. (c) Tomographic slice of the calcification with the concentric laminations in the internal structure. (d) Large conglomerate of calcifications. (e) Tomographic slice of the conglomerate with a noticeable layered structure at the edges. (f) Large conglomerate of calcification within the soft tissue. (g) Tomographic slice of the soft tissue next to the conglomerate.

parameters.

5. Conclusion

We believe that our research affords a new insight into studies on the structures and functions of neuroendocrine PG while providing the high-quality and high-resolution 3D image of the whole uncut and unstained post-mortem organ. Progress in this field is currently hindered by a lack of non-invasive high-resolution imaging techniques. We have shown that XPCT produces highly informative 3D visualization of PG soft and calcified tissue with near histological morphological features, which are essential in the understanding of PG individual variability and PG pathology. In particular, we have shown that XPCT allows nondestructive detection of calcifications and soft tissue lesions in PG. XPCT clearly distinguishes between the intact PG tissue and the gliosis surrounding cysts with the histological details such as pinealocytes with their nuclei in the parenchyma and the glial cells processes in the cystic glial tissue.

Funding

Consiglio Nazionale delle Ricerche ("Accordo Bilaterale CNR/RFBR 2018–220" CUP B86C17000210005) & Russian Foundation for Basic Research (18-52-7819); MIUR-CNR ("Tecnopolo diNanotecnologia e Fotonica per la Medicina di Precisione"CUPB83B17000010001) & Regione Puglia ("Tecnomed" CUP B84I18000540002).

Declaration of Competing Interest

The authors declare that they have no known competing financial interests or personal relationships that could have appeared to influence

the work reported in this paper.

Acknowledgements

The bilateral project CNR/RFBR (2018- 2020) - accordo CNR-RFBR delle Relazioni Internazionali (CUP B86C17000210005 & Russian number 18-52-7819), the national project RFBR (number 18-29-26028)-Russian Federation, the FISR Project "Tecnopolo di nanotecnologia e fotonica per la medicina di precisione" (funded by MIUR/CNR, CUP B83B17000010001) and the TECNOMED project (funded by Regione Puglia, CUP B84I18000540002) are acknowledged for financial support. We also thank the Ministry of Science and Higher Education of Russian Federation within the State assignment FSRC «Crystallography and Photonics» RAS for financial supporting and for the use of equipment of the Shared Research Center "Structural diagnostics of materials" (project RFMEFI62119X0035). M. Fratini acknowledges the Italian Ministry of Health Young Researcher Grant 2013 (GR-2013-02358177) for financial support.

The authors thank the staff of the P05 beamline Fabian Wilde and Elena Longo at the P05 beamline of the synchrotron facility PETRA III, DESY, operated by the Helmholtz-Zentrum Geesthacht and Alberto Bravin at ID17 at ESRF for their experimental support.

Authors contributions

I.B., O.J., M.F., A.C., A.I.,V.A., S. S. wrote the main manuscript text; M.F., I.B., F.P., L.M, G.B.P., N.P. A.S., A.B., Yu..K., D.Z., O.J. carried out XPCT experiment, A.B. and Yu.K. carried out micro-CT experiment, I.B. and M.F. performed XPCT data processing, I.B. performed XPCT image processing, A.B., Yu.K., A.I., M.C. performed micro-CT data and image processing and analysis, O.J., D.A.O., S.S. performed the histological examination and provided histological images of PGs, O.J., S.S. performed micro-CT, XPCT image analysis. All authors reviewed the manuscript.

Appendix A. Supplementary data

Supplementary data to this article can be found online at https://doi.org/10.1016/j.jsb.2020.107659.

References

Alcolado, J.C., Moore, I.E., Weller, R.O., 1986. Calcification in the human choroid plexus, meningiomas and pineal gland. Neuropathol. Appl. Neurobiol. 12, 235–250.

Bravin, A., Coan, P., Suortti, P., 2013. X-ray phase-contrast imaging: from pre-clinical applications towards clinics. Phys. Med. Biol. 58, R1–R35. https://doi.org/10.1088/0031-9155/58/1/R1 PM-23220766.

Brun, F., Massimi, L., Fratini, M., Dreossi, D., Billé, F., Accardo, A., Pugliese, R., Cedola, A., 2017. SYRMEP Tomo Project: a graphical user interface for customizing CT reconstruction workflows. Adv. Struct. Chem. Imaging 3, 4. https://doi.org/10.1186/s40679-016-0036-8.

Bruno, F., Arrigoni, F., Maggialetti, N., Natella, R., Reginelli, A., Di Cesare, E., Brunese, L., Giovagnoni, A., Masciocchi, C., Splendiani, A., Barile, A., 2019. Neuroimaging in emergency: A review of possible role of pineal gland disease. Gland Surg. https://doi.org/10.21037/gs.2019.01.02.

Buzmakov, A.V., Asadchikov, V.E., Zolotov, D.A., Roshchin, B.S., Dymshits, Y.M., Shishkov, V.A., Chukalina, M.V., Ingacheva, A.S., Ichalova, D.E., Krivonosov, Y.S., Dyachkova, I.G., Balzer, M., Castele, M., Chilingaryan, S., Kopmann, A., 2018. Laboratory microtomographs: design and data processing algorithms. Crystallogr. Reports 63, 1057–1061. https://doi.org/10.1134/S106377451806007X M4.

Cedola, A., Bravin, A., Bukreeva, I., Fratini, M., Pacureanu, A., Mittone, A., Massimi, L., Cloetens, P., Coan, P., Campi, G., Spanò, R., Brun, F., Grigoryev, V., Petrosino, V., Venturi, C., Mastrogiacomo, M., Kerlero De Rosbo, N., Uccelli, A., 2017. X-Ray phase contrast tomography reveals early vascular alterations and neuronal loss in a multiple sclerosis model. Sci. Rep. 7, 1–11. https://doi.org/10.1038/s41598-017-06251-7.

Erlich, S.S., Apuzzo, M.L., 1985. The pineal gland: anatomy, physiology, and clinical significance. J. Neurosurg. 63, 321–341. https://doi.org/10.3171/jns.1985.63.3.0321 PM-2862230 M4.

Fratini, M., Bukreeva, I., Campi, G., Brun, F., Tromba, G., Modregger, P., Bucci, D., Battaglia, G., Spanò, R., Mastrogiacomo, M., Requardt, H., Giove, F., Bravin, A., Cedola, A., 2015. Simultaneous submicrometric 3D imaging of the micro-vascular network and the neuronal system in a mouse spinal cord. Sci. Rep. 5, 8514. https://doi.org/10.1038/srep08514 PM-25686728.

Golan, J., Torres, K., Staśkiewicz, G.J., Opielak, G., Maciejewski, R., 2002. Morphometric parameters of the human pineal gland in relation to age, body weight and height. Folia Morphol. (Warsz) 61, 111–113.

Goldman, H., Wurtman, R.J., 1964. Flow of blood to the pineal body of the rat. Nature 203, 87–88. https://doi.org/10.1038/203087a0.

Khimchenko, A., Bikis, C., Pacureanu, A., Hieber, S.E., Thalmann, P., Deyhle, H., Schweighauser, G., Hench, J., Frank, S., Müller-Gerbl, M., Schulz, G., Cloetens, P., Müller, B., 2018. Hard X-ray nanoholotomography: large-scale, label-free, 3D neuroimaging beyond optical limit. Adv. Sci. 5, 1700694. https://doi.org/10.1002/advs.201700694.

Kim, J., Kim, H.W., Chang, S., Kim, J.W., Je, J.H., Rhyu, I.J., 2012. Growth patterns for acervuli in human pineal gland. Sci. Rep. 2 (984), 1–6. https://doi.org/10.1038/srep00984.

Koshy, S., Vettivel, S.K., 2001. Varying appearances of calcification in human pineal gland: a light microscopic study. J. Anat. Soc. India 50, 17–18.

Kunz, D., Schmitz, S., Mahlberg, R., Mohr, A., Stöter, C., Wolf, K.J., Herrmann, W.M., 1999. A new concept for melatonin deficit: On pineal calcification and melatonin excretion. Neuropsychopharmacology 21, 765–772. https://doi.org/10.1016/S0893-133X(99)00069-X.

Massimi, L., Bukreeva, I., Santamaria, G., Fratini, M., Corbelli, A., Brun, F., Fumagalli, S., Maugeri, L., Pacureanu, A., Cloetens, P., Pieroni, N., Fiordaliso, F., Forloni, G., Uccelli, A., Kerlero de Rosbo, N., Balducci, C., Cedola, A., 2019. Exploring Alzheimer's disease mouse brain through X-ray phase contrast tomography: From the cell to the organ. Neuroimage 184, 490–495. https://doi.org/10.1016/j.neuroimage.2018.09.044.

Mittone, A., Manakov, I., Broche, L., Jarnias, C., Coan, P., Bravin, A., 2017. Characterization of a sCMOS-based high-resolution imaging system. J. Synchrotron Radiat. 24, 1226–1236. https://doi.org/10.1107/S160057751701222X.

Pacilè, S., Dullin, C., Baran, P., Tonutti, M., Perske, C., Fischer, U., Albers, J., Arfelli, F., Dreossi, D., Pavlov, K., Maksimenko, A., Mayo, S.C., Nesterets, Y.I., Taba, S.T., Lewis, S., Brennan, P.C., Gureyev, T.E., Tromba, G., Wienbeck, S., 2019. Free propagation phase-contrast breast CT provides higher image quality than cone-beam breast-CT at low radiation doses: a feasibility study on human mastectomies. Sci. Rep. 9, 1–7. https://doi.org/10.1038/s41598-019-50075-6.

Paganin, D., Mayo, S.C., Gureyev, T.E., Miller, P.R., Wilkins, S.W., 2002. Simultaneous phase and amplitude extraction from a single defocused image of a homogeneous object. J. Microsc. 206, 33–40. https://doi.org/10.1046/j.1365-2818.2002.01010.x PM-12000561.

Schindelin, J., Arganda-Carreras, I., Frise, E., Kaynig, V., Longair, M., Pietzsch, T., Preibisch, S., Rueden, C., Saalfeld, S., Schmid, B., Tinevez, J.-Y., White, D.J., Hartenstein, V., Eliceiri, K., Tomancak, P., Cardona, A., 2012. Fiji: an open-source platform for biological-image analysis. Nat. Methods 9, 676–682. https://doi.org/10.1038/nmeth.2019 PM-22743772.

Schmid, H.A., 1993. Decreased melatonin biosynthesis, calcium flux, pineal gland calcification and aging: A hypothetical framework. Gerontology. https://doi.org/10.1159/000213533.

Song, J., 2019. Pineal gland dysfunction in Alzheimer's disease: Relationship with the immune-pineal axis, sleep disturbance, and neurogenesis. Mol. Neurodegener. https://doi.org/10.1186/s13024-019-0330-8.

Tan, D., Xu, B., Zhou, X., Reiter, R., 2018. Pineal calcification, melatonin production, aging, associated health consequences and rejuvenation of the pineal gland. Molecules 23, 301. https://doi.org/10.3390/molecules23020301.

Töpperwien, M., van der Meer, F., Stadelmann, C., Salditt, T., 2020. Correlative x-ray phase-contrast tomography and histology of human brain tissue affected by Alzheimer's disease. Neuroimage 210, 116523. https://doi.org/10.1016/j.neuroimage.2020.116523.

van Aarle, W., Palenstijn, W.J., Beenhouwer, J., Altantzis, T., Bals, S., Batenburg, K.J., Sijbers, J., 2015. The ASTRA Toolbox: A platform for advanced algorithm development in electron tomography. Ultramicroscopy 157, 35–47. https://doi.org/10.1016/j.ultramic.2015.05.002 PM-26057688.

Wang, G., 2002. X-ray micro-CT with a displaced detector array. Med. Phys. 29, 1634–1636. https://doi.org/10.1118/1.1489043.

Wilde, F., Ogurreck, M., Greving, I., Hammel, J.U., Beckmann, F., Hipp, A., Lottermoser, L., Khokhriakov, I., Lytaev, P., Dose, T., Burmester, H., Müller, M., Schreyer, A., 2016. Micro-CT at the imaging beamline P05 at PETRA III. In: AIP Conference Proceedings. American Institute of Physics Inc., p. 030035 https://doi.org/10.1063/1.4952858.